PNAS RESEARCH ARTICLE | BIOPHYSICS AND COMPUTATIONAL BIOLOGY OPEN ACCESS

Oligomerization-driven avidity correlates with SARS-CoV-2 cellular binding and inhibition

Roi Asor[a,b], Anna Olerinyova[a,b], Sean A. Burnap[b,c], Manish S. Kushwah[a,b], Fabian Soltermann[a,b], Lucas S.P. Rudden[d], Mario Hensen[b,c], Snežana Vasiljevic[b,c], Juliane Brun[b,c], Michelle Hill[b,c], Liu Chang[e,f], Wanwisa Dejnirattisai[e,g], Piyada Supasa[e], Juthathip Mongkolsapaya[e,f], Daming Zhou[h], David I. Stuart[h,i], Gavin R. Screaton[e,j], Matteo T. Degiacomi[d], Nicole Zitzmann[b,c], Justin L. P. Benesch[a,b], Weston B. Struwe[b,c,1], and Philipp Kukura[a,b,1]

Affiliations are included on p. 10.

Edited by Pamela Bjorkman, California Institute of Technology, Pasadena, CA; received February 20, 2024; accepted June 28, 2024

Cellular processes are controlled by the thermodynamics of the underlying biomolecular interactions. Frequently, structural investigations use one monomeric binding partner, while ensemble measurements of binding affinities generally yield one affinity representative of a 1:1 interaction, despite the majority of the proteome consisting of oligomeric proteins. For example, viral entry and inhibition in SARS-CoV-2 involve a trimeric spike surface protein, a dimeric angiotensin-converting enzyme 2 (ACE2) cell-surface receptor and dimeric antibodies. Here, we reveal that cooperativity correlates with infectivity and inhibition as opposed to 1:1 binding strength. We show that ACE2 oligomerizes spike more strongly for more infectious variants, while exhibiting weaker 1:1 affinity. Furthermore, we find that antibodies use induced oligomerization both as a primary inhibition mechanism and to enhance the effects of receptor-site blocking. Our results suggest that naive affinity measurements are poor predictors of potency, and introduce an antibody-based inhibition mechanism for oligomeric targets. More generally, they point toward a much broader role of induced oligomerization in controlling biomolecular interactions.

label-free single-molecule tracking | mass photometry | SARS-CoV-2 | receptor oligomerization | avidity-based neutralization potency

Significance

Viral entry is mediated by interactions between multivalent proteins, which are difficult to capture with current structural and biophysical methods owing to the underlying heterogeneity and requirement for a membrane surface. Here, we use mass photometry to quantify severe acute respiratory syndrome coronavirus 2 (SARS-CoV-2) interaction and inhibition taking place in solution and on lipid membranes. We show that multivalency and cooperativity control the spike–angiotensin-converting enzyme 2 (ACE2) interactions making the general reduction to a 1:1 interaction model inadequate to capture the underlying molecular dynamics. We find evidence for ACE2 inducing spike oligomerization in a variant-dependent manner that enhances its cellular affinity by driving receptor clustering. In addition, induced oligomerization emerges as a fundamental mode of action of antibodies, operating on its own, or combined with traditional receptor blocking.

Successful viral entry requires efficient engagement of receptors on the host cell by proteins on the virus surface (1). Such interactions are targeted both by some aspects of the host immune system and various antiviral therapeutics, in an effort to outcompete the native association. Most proteins on the virus and cell surfaces are oligomeric, and therefore the underlying molecular interactions between them offer great scope for both the virus and immune system to leverage the thermodynamic benefits of multivalent binding (2–7). While there is a growing appreciation of the importance of multivalency, over and above the strength of the constituent interfaces, its visualization and quantification are challenging due to the inevitable heterogeneity of assembly states it gives rise to.

SARS-CoV-2 infection and inhibition represent an archetypal system for studying multivalency: It involves a trimeric viral envelope fusion spike protein (8) that attaches to a dimeric angiotensin-converting enzyme 2 (ACE2) on host cells (6) (Fig. 1*A*). The important role multivalency plays is exemplified by the emergence of ACE2 as an early potential therapeutic (9), where the dimeric form exhibits strongly enhanced binding to spike and a much lower IC50 compared to monomeric ACE2 (10–12). These results point toward avidity effects: Dimerization of ACE2 results in tighter binding than can be explained by simple combination of two monomers. Essentially equivalent observations have been made in the context of antibody efficacy, where stark differences have been observed between intact IgG antibodies and single Fabs (5, 13–15). As for ACE2, multivalency is an important consideration for antibodies, given that they are composed of an Fc region fused to two identical Fabs effectively acting as covalent dimers.

Despite this strong evidence for the involvement and significant influence of multivalency on both SARS-CoV-2 host cell binding (4, 6) and inhibition of viral infection by antibodies more broadly (3), insight into its strength, and how it depends on different virus variants and antibody identity, is absent. The reason for this is that structural and biophysical characterization often relies on simplifying the system by reduction to monomeric interactions. For instance, structures relevant to the spike–ACE2 interaction have been solved largely for scenarios where one of the binding partners is engineered to be monomeric, while quantification of affinities is interpreted within a simple 1:1 binding model, such that any avidity effects are hidden within an apparent enhancement of the observed binding affinity. For

This article is a PNAS Direct Submission.

Copyright © 2024 the Author(s). Published by PNAS. This open access article is distributed under Creative Commons Attribution License 4.0 (CC BY).

[1]To whom correspondence may be addressed. Email: weston.struwe@chem.ox.ac.uk or philipp.kukura@chem.ox.ac.uk.

This article contains supporting information online at https://www.pnas.org/lookup/suppl/doi:10.1073/pnas.2403260121/-/DCSupplemental.

Published September 19, 2024.

Downloaded from https://www.pnas.org by 46.64.248.158 on October 11, 2024 from IP address 46.64.248.158.

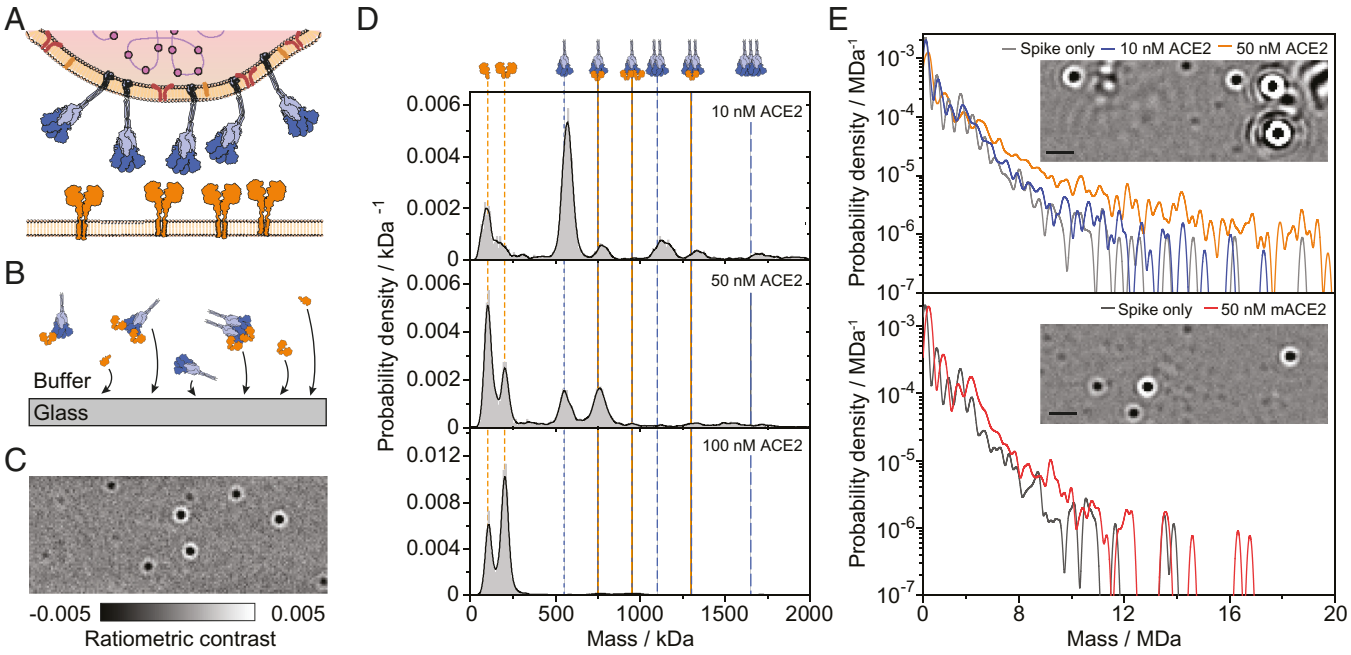

Fig. 1. ACE2 induces oligomerization of spike trimers in solution. (*A*) Schematic of the multivalent interaction partners at the SARS-CoV2 virus–cell interface, containing viral trimeric spike glycoproteins and dimeric ACE2 on the surface of the host cell. (*B*) The detection principle of solution-based mass photometry, relying on nonspecific binding of soluble proteins to a glass surface. (*C*) Resulting MP images of individual complexes from a spike–ACE2 mixture. (Scale bar: 1 μm.) (*D*) Mass histograms of spike–ACE2 mixtures. Spike trimers at 0.55 μM were incubated in the presence of 0.33 to 3.3 μM ACE2 for 10 min at ambient room temperature, and then rapidly diluted to the working concentration of MP just before data acquisition (see *SI Appendix*, Fig. S1 for measurement of incubated spike at the same conditions without added ACE2). The final concentration of spike trimer was 16.7 nM. Vertical lines indicate the masses of the expected molecular complexes. Histograms were generated by combining 3 to 6 technical replicates. The total number of particles were 12,430, 28,246, and 86,390 for samples containing 10, 50, and 100 nM ACE2, respectively. (*E*) Mass histograms, for mixing spike trimers with ACE2 (*Top*) and monomeric ACE2 (mACE2, *Bottom*), presented on a semilogarithmic scale, showing the increase in the solution concentration of large spike–ACE2 complexes. The probability density was calculated using kernel width of 100 kDa and included all particles larger than 450 kDa to exclude the varying contribution of free ACE2. Insets show representative frames of the recorded MP video of spike with 50 nM ACE2 and 50 nM mACE (Scale bar: 1 μm).

neutralizing antibodies, the potential of intraspike avidity was predicted (16) and also suggested by resolving cryoelectron microscopy (cryo-EM) structures showing configurations of multi-receptor binding domain (RBD) bound to multi-Fab domains (13). Interestingly, however, among the different antibodies whose structures were resolved, the most potent neutralizing antibody was found to bind monovalently, indicating that intraspike avidity was not possible, despite an almost three orders of magnitude difference in neutralization potency between the Fab and the full IgG (13). Recent studies using native mass spectrometry (17) and mass photometry (MP) (18–20) have found signatures of both antibodies and ACE2-producing complexes consistent with oligomerization of spike, but have either been neglected, not quantified or not interpreted in the context of infectivity and inhibition. In fact, the interpretation of these results remained within the classic 1:1 interaction framework, focusing on avidity effects corresponding to intraspike interactions. As a result, despite a tremendous number of studies emerging over the past few years aimed at understanding the connection between affinity, infectivity, and inhibition for SARS-CoV2, no clear picture as to the role and importance of oligomerization has emerged (12, 21–27).

To address these shortcomings, we designed an approach based on MP (28) that enables us to observe and quantify receptor–ligand interactions at the molecular level, both free in solution and confined to lipid bilayers (29, 30) that mimic the surface membrane of the virus and host cells. The mass resolution and single-molecule sensitivity of MP enable digital counting of individual proteins and their complexes, which can then be separated into affinities for each elementary step within the coupled equilibria that comprise the heterogeneous system (31) rather than aggregating them into a 1:1 binding model. We find that induced-oligomerization and cooperativity can be directly observed and quantified from the resulting mass distributions for spike and ACE2 or antibodies. This allows us to pinpoint the precise molecular steps that are leveraged by the virus and immune system for efficient association with the cell, or its inhibition, revealing a central role of induced oligomerization for both cellular binding and antibody-based inhibition.

Results

We begin by characterizing the interactions that occur in solution, for which we use a standard MP assay, where protein complexes binding nonspecifically from solution to a glass surface are mass-measured from their images (Fig. 1 *B* and *C*). Quantifying the contrast of each binding event together with a mass calibration results in mass distributions representative of protein complexes present in solution. For our Wuhan-Hu-1 spike construct (wtSpike), we find a major species near the expected 550 kDa trimer mass, as well as additional peaks corresponding to higher oligomers of the trimer (*SI Appendix*, Fig. S1*A*). Small deviations (up to 2%) in the accuracy of the measured mass are expected owing to small experimental variations of the optical contrast to mass conversion calibration arising from experiment-to-experiment variations in focus position (28). Performing such experiments for mixtures of ACE2 and RBD yields the full interaction landscape, with a binding affinity of 28 ± 9 nM between a single RBD and an individual ACE2 binding site (*SI Appendix*, Fig. S2), in excellent agreement with previous results (8, 12, 21, 24, 32–34). These results demonstrate the validity of our method to identify different oligomeric species, their binding to ligands and thus to quantify affinities with stoichiometric resolution.

Downloaded from https://www.pnas.org by 46.64.248.158 on October 11, 2024 from IP address 46.64.248.158.

ACE2 Induces Oligomerization of wtSpike in Solution. Equipped with these capabilities, we turned to quantify the interaction between the oligomeric binding partners, namely the solubilized versions of wtSpike and ACE2. Previous studies have reported extremely tight binding affinities on the order of few nM or less (12, 25, 35, 36). Measurements of 50 nM wtSpike (16.7 nM wtSpike trimers) at 1:1.67 and 3:1 ACE2 to wtSpike trimer ratios after incubation at μM concentration revealed binding of 1 and 2 ACE2 to the wtSpike trimer, and oligomers thereof (Fig. 1*D* and *SI Appendix*, Fig. S1). Interestingly, under both conditions, we found clear signatures of free ACE2 and spike trimer, pointing toward a much weaker binding affinity (>40 nM) compared to those previously reported. The changeover from predominantly monomeric to dimeric ACE2 in solution over the explored concentration range is expected based on our measured K_D (12 ± 2 nM, *SI Appendix*, Fig. S2 and Table S1).

At a 6:1 ACE2:wtSpike trimer ratio, we observed a dramatic decrease in the number of detected spike-containing species in the <2 MDa mass range, indicating almost complete loss of wtSpike from solution. Inspection of the resulting MP images revealed signatures exhibiting very large optical contrast that must stem from more massive particles than those generated by wtSpike trimers alone (Fig. 1 *E*, *Inset* and Movie S1). These are very low in abundance, so the single-particle sensitivity of MP is highly advantageous because it provides in principle unlimited dynamic range for detection and quantification, including of large complexes. Indeed, when plotting the mass distributions from these experiments on a logarithmic abundance scale, we find a long tail of large oligomers with masses >4 MDa that increases with increasing ACE2 to wtSpike ratio persisting all the way to 20 MDa (Fig. 1*E* and *SI Appendix*, Figs. S1 *B* and *C* and S3). It is important to note that oligomerization of spike by ACE2 relies both on the fundamental affinity of ACE2 to spike and the cross-linking propensity of ACE2. Since it is a collective process, it will inevitably be related to the concentration of spike trimer. On the surface of the virus, spike trimers are found at a very high density (about 1,000 μm^{-2}, 37). Any attempt to observe effects relevant to such densities thus requires high solution concentrations of the interacting subunits.

To further evaluate whether the occurrence of these large objects arises from induced oligomerization of wtSpike by ACE2, we repeated these experiments under similar conditions with mACE2. The resulting MP images now resembled those for wtSpike-only (Fig. 1 *E*, *Inset*), without any significant increase in the abundance of species of mass >4 MDa. Taken together, these results suggest that ACE2 induces oligomerization of wtSpike in solution. They may also help explain the lack of structural studies using spike trimers and dimeric ACE2, because this combination at high concentrations leads to a heterogeneous mixture that is not suitable to single-particle averaging required for cryoelectron microscopy. Importantly, induced oligomerization explains the discrepancy between our observation of a relatively weak ACE2-wtSpike interaction (>40 nM) and previous reports (<3 nM) obtained with traditional assays. This is likely due to the fact that such surface-based assays use a dense layer of one of the ligands, which is intrinsically subject to avidity effects when interacting with oligomeric ligands from solution (similar to increasing the total solution concentration in solution-based assays). Our results call for a reevaluation of both the interaction strength between spike and ACE2, as well as more generally questioning the suitability of standard surface-based assays when using oligomeric interaction partners, importantly including full-length antibodies.

Induced Oligomerization of Spike by ACE2 Proceeds on Bilayer Membranes. These experiments demonstrate that ACE2 induces oligomerization of spike in solution, but cannot reveal the associated energetics, nor does it resemble the membrane-associated nature of the interacting species and the effect of reduced dimensionality on their interactions (38). To address this, we turned to an alternative approach to MP, based on tracking individual proteins diffusing on supported lipid bilayers (29, 30). We attach individual spike trimers to lipids in the bilayer membrane using a 6×His tag-NTA(Ni) linkage (Fig. 2*A*), and then follow their motion and mass as a function of time (Fig. 2*B* and Movie S2). In this way, we can monitor individual spike trimers for extended periods of time, measuring their mass continuously on a frame-by-frame basis (Fig. 2*C*). The observed mass fluctuations are a consequence of the high frame rate required to minimize motional blurring (270 Hz) as seen by the overlay of the measurement noise distribution (Fig. 2*C*), rather than actual mass fluctuations of the complexes (*SI Appendix*, Fig. S4).

The ability to identify and localize individual trimers as a function of time also enables us to quantify their mobility. Plotting the cumulative distribution function of observed step sizes yields an accurate estimate of the diffusion coefficient, on a trimer-by-trimer basis through appropriate fitting (Fig. 2*D*). The measurement precision for individual complexes is mainly limited by trajectory length, which is determined by the achievable field of view, the mobility, and our ability to link trajectories in the presence of many molecules simultaneously diffusing on the bilayer. The observed mobilities are Brownian in nature, as expected for individual lipids diffusing in an idealized bilayer membrane.

We can then combine the resulting mass and mobility measurements from individual recordings to assess the overall behavior of the system, where each data point in the two-dimensional scatter plot corresponds to a single trajectory (Fig. 2 *E*–*G*). For wtSpike in the absence of ACE2, we find highly homogeneous behavior, dominated by individual trimers with an average mass of 494 kDa diffusing with D = 1.2 ± 0.3 $\mu m^2/s$. The measured mass on the bilayer is slightly lower than that obtained from a regular MP assay (548 kDa), because of the effective height and flexibility of the spike trimer as it tethered on the surface of the bilayer. This leads to variations in the optical pathlength (additional phase shift) between reflected and scattered light that forms the basis of the optical contrast in MP, with the consequence of lowering the optical contrast independent of focus position (see *SI Appendix* and *SI Appendix*, Fig. S5 for a detailed discussion). We measured and corrected this variation using measurements on glass and comparison with a calibration protein on the supported lipid bilayer (*SI Appendix*, Fig. S5), resulting in corrected mass histograms (Fig. 2 *E*–*G*). The mass distribution of species is now dominated by trimers, because the bilayer serves to specifically pull down his-tagged species, and noncovalent oligomers of trimers likely disassemble during the experiment, possibly owing to the more strict orientational constraints for binding when spike proteins are tethered to the bilayer compared to free rotation in solution.

Following the tethering of spike to the bilayer, the addition of 100 nM ACE2 causes clear changes to these distributions. As expected from our solution-based measurements, we now observe wtSpike with 0, 1, and 2 ACE2 bound, but with a clear additional distribution above 1 MDa in the region expected for dimers of spike cross-linked and bound by ACE2, which is also associated with a drop in the diffusion coefficient (Fig. 2*F*). These species appear at a mass in good agreement with the expected mass for the respective spike–ACE2 oligomers, which are evident in both the individual trajectories, and when inspecting the overall

Downloaded from https://www.pnas.org by 46.64.248.158 on October 11, 2024 from IP address 46.64.248.158.

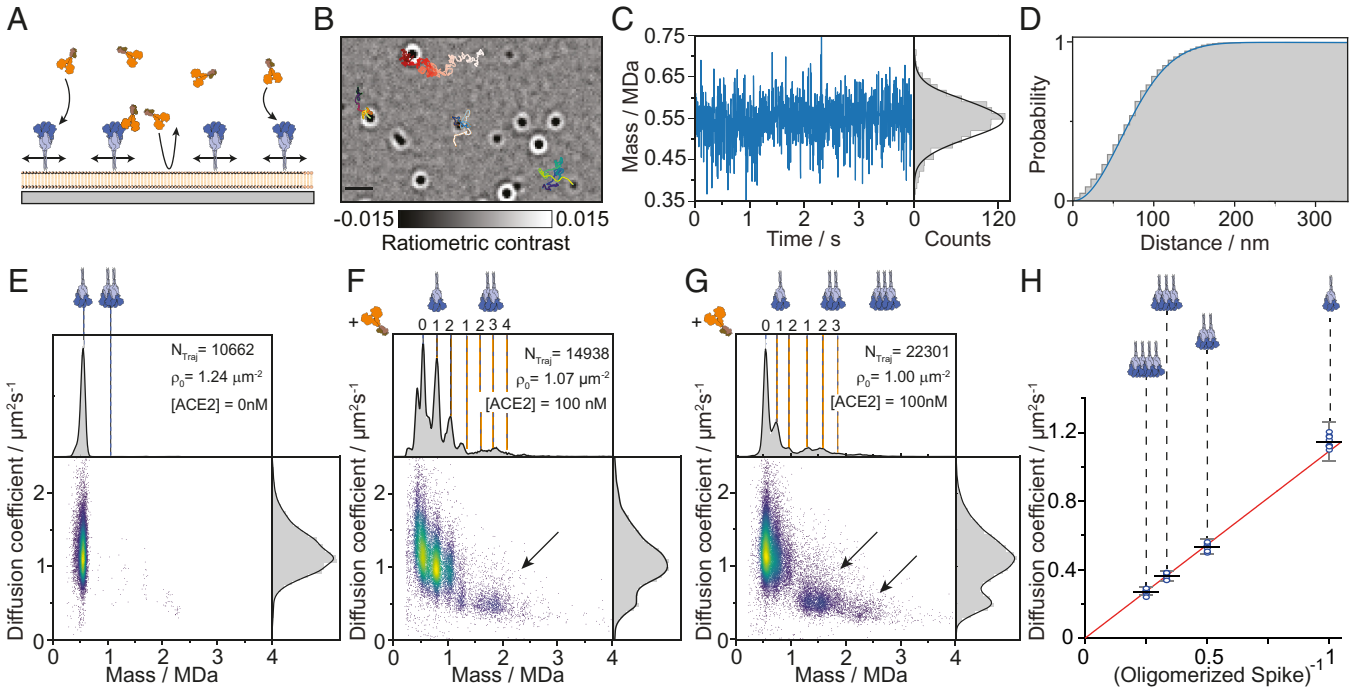

Fig. 2. Single-particle tracking and mass measurement reveal ACE2-induced oligomerization of spike trimers on supported lipid bilayers. (*A*) Schematic of the assay with bilayer-tethered spike trimers and ACE2 binding from solution. The supported lipid bilayers also serve as a passivation layer keeping the concentration of ACE2 constant in solution. (*B*) Representative frame from a median ratiometric video, including trajectories for a few particles. The color gradient corresponds to trajectory propagation time. (*C*) Representative recorded single-particle mass trace, and the corresponding mass histogram of an individual spike trimer measured at 270 Hz (gray). The black curve corresponds to the intrinsic measurement noise distribution in mass units. The distribution was shifted to be centered at the average particle mass. (*D*) Cumulative probability distribution of the distance traveled by a single spike trimer during a single frame within its measured trajectory. The corresponding time interval for particle displacement was 3.7 ms. The blue curve corresponds to the best-fitted model used to extract the diffusion coefficient (*SI Appendix*, section *Generating 2D Mass-Diffusion Plots*). (*E–G*) Two-dimensional plots of the measured diffusion coefficient *vs.* average mass of individual trajectories (scatter points) for (*E*) wtSpike following equilibration for a few hours on the supported lipid bilayer, (*F*) wtSpike and (*G*) omSpike, both following equilibration with 100 nM ACE2. The expected masses for different stoichiometries are indicated by vertical lines. The numbers above the vertical lines indicate the number of bound ACE2 to spike trimer and to cross-linked dimer of trimers. The number of trajectories recorded for each condition (N_{traj}) and detected initial surface density of spike (ρ_0) are stated in each panel. Arrows indicate the regions in the two-dimensional plot where the measured diffusion and mass values are expected for trajectories that correspond to complexes of oligomerized spike trimers. (*H*) Measured diffusion coefficient *vs.* the inverse of spike cluster size for tethered wtSpike. Circles indicate the diffusion coefficient estimate based on a two-dimensional Gaussian mixture model from eight independent experiments (*SI Appendix*, Fig. S6), black bars and error bars correspond to the averages and their SD. Error bars for individual circles are not shown for clarity. The red line corresponds to a linear fit with the intercept set to the origin.

envelope of measured diffusion coefficients. Repeating these experiments at similar ACE2 concentration and spike density with the Omicron variant of spike (omSpike) results in much more extensive (and rapid) oligomerization (Movie S3), including signatures consistent with ACE2 decorated spike trimers (Fig. 2*G*). This increase in oligomerization propensity is also evident in the rise of the low mobility shoulder in the overall envelope of measured diffusion coefficients. Interestingly, omSpike exhibits a higher tendency to oligomerize upon ACE2 binding despite a lower occupancy on free spike trimer, which suggests a lower 1:1 affinity.

The simultaneous measurement of mass and mobility of individual spike complexes in the presence of ACE2 on lipid bilayers provides further evidence for ACE2-induced oligomerization of spike. Species consistent with a dimer of spike exhibit roughly half the mobility of the monomer, with a further proportional reduction observable for the trimer, and even tetramer. Plotting the diffusion coefficient as a function of the reciprocal of the number of spike trimers yields a linear relationship (Fig. 2*H* and *SI Appendix*, Fig. S6). Such behavior is expected for a digital increase in the number of bound lipids per complex, with larger oligomers slowing down due to the increase in drag experienced by multiple lipids incorporated into the bilayer membrane. The combined measurement of mass and diffusion can also explain the observed additional unassigned peaks in Fig. 2*F* that we relate to a small fraction of dimers and monomers of spike that always coexist with the trimeric form of spike in solution (for our wtSpike construct stabilized by two proline substitutions as shown in *SI Appendix*, Figs. S7 and S8 and also in ref. 39). These cannot be detected in the initial distribution (Fig. 2*E*) owing to their lower mass that is close to the detection limit (monomer) and their low abundance relative to the trimer (dimer). However, these can reappear when ACE2 is added to solution following their interaction with ACE2 and the lower abundance of free wtSpike trimer.

Binding of ACE2 to Spike Exhibits Variant-Dependent Cooperativity. Our results demonstrate that ACE2 oligomerizes spike both in solution and on lipid bilayers and suggest that the ACE2:spike interaction is much weaker than previously reported. At the same time, we have not yet provided a full quantification of the molecular interactions with stoichiometric resolution. To take advantage of this unique capability of MP, we repeated the experiments reported in Fig. 1, but mixed ACE2 and spike at nM concentration, which enables us to avoid the formation of large oligomers and loss of spike from solution (Fig. 1), while maintaining high mass resolution to accurately separate binding stoichiometries. For mACE2, we find clear signatures of 1 to 3 bound mACE2 to spike, with the abundance of higher occupancy increasing as expected with mACE2 concentration (Fig. 3*A* and *SI Appendix*, Fig. S7). Quantifying the fractional occupancy of each binding site enables us to fit the data globally, yielding K_D = 170 ± 5 nM (see *SI Appendix*, *Distribution Analysis of Solution Mass Measurement* for a description of the fitted model). Fitting the data to a model allowing for cooperativity between the three binding

Downloaded from https://www.pnas.org by 46.64.248.158 on October 11, 2024 from IP address 46.64.248.158.

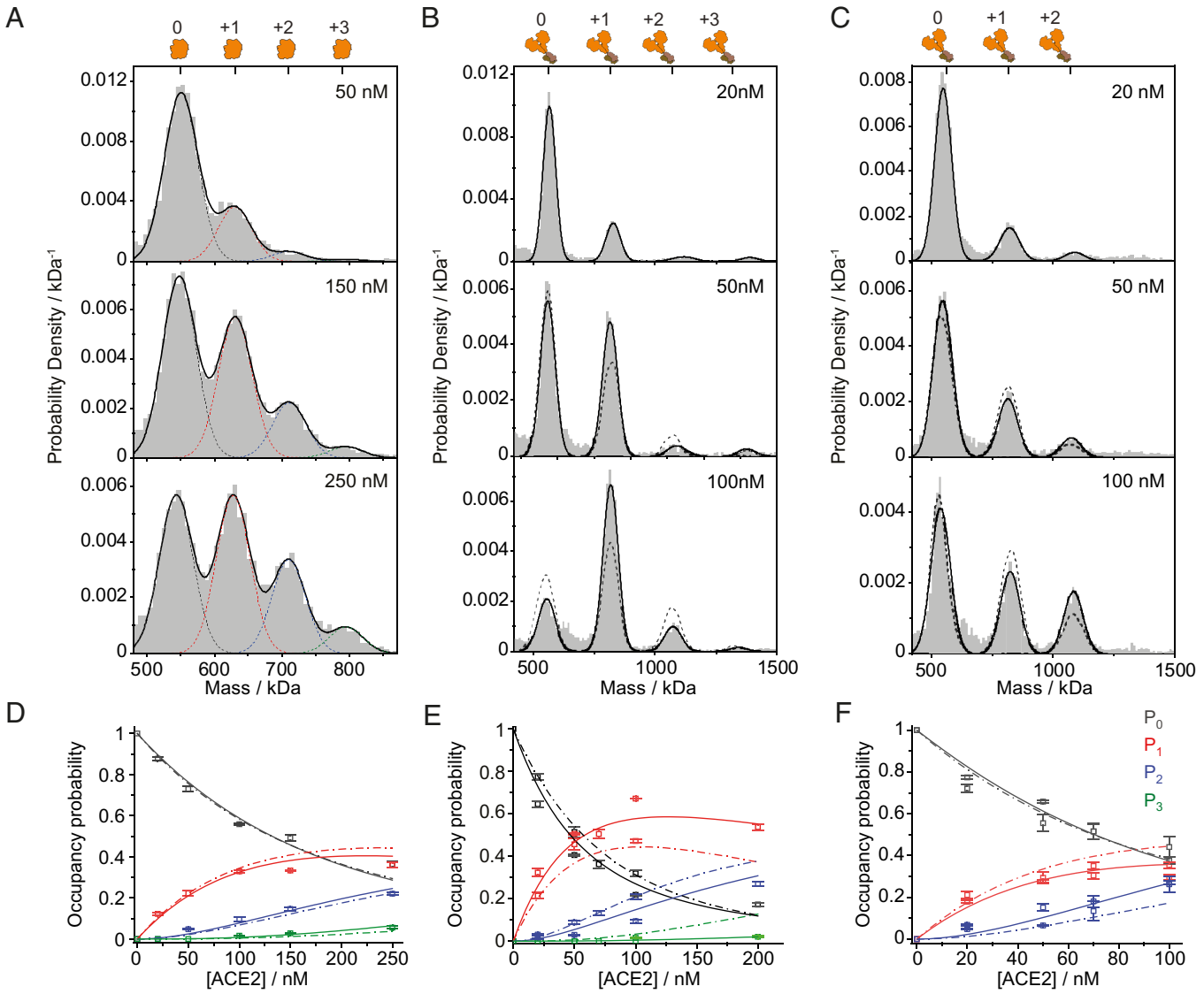

Fig. 3. Thermodynamic analysis of the spike–ACE2 interaction in solution reveals variant-specific cooperativity. (*A*–*C*) Normalized mass distributions for mixtures of 25 nM wtSpike with increasing concentrations of (*A*) mACE2 and (*B*) ACE2, and 25 nM omSpike with increasing concentrations of ACE2 (*C*). Histograms represent cumulative counts of 3 to 5 technical repeats per mixture. The black solid curve corresponds to the modeled distribution based on a fitted sum of Gaussian functions. For overlapping peaks in (*A*), the individual Gaussian functions are shown. Gaussian functions were constrained to the expected masses of the individual complexes and to their expected experimental mass SD. The expected positions of the different spike:ACE2 stoichiometries are indicated at the *Top* of each panel. (*D*–*F*) The resolved occupancy probabilities (scatter points) based on the fitted Gaussian functions for spike with 0 (free spike, P_0 and gray symbols), 1 to 3 bound (P_{1-3}, labeled as red, blue, and green, respectively) (*D*) mACE2, (*E*) ACE2 to wtSpike and (*F*) ACE2 to omSpike as a function of ACE2 concentration. Individual scatter symbols and error bars correspond to the average values of 3 to 5 technical replicates and their SD, respectively. For wtSpike and omSpike interactions with dimeric ACE2, the scatter points include results from two biological replicates (*Material and Methods* section). Solid lines correspond to the expected occupancies based on the globally best fitted thermodynamic model. The model takes into account a fundamental standard free energy change for interaction between individual RBD site and ACE2 monomer, $\Delta G°$, the degeneracy of the multivalent subunits, and an effective free energy term to account for cooperativity between RBDs on the same spike trimer, $\delta\Delta G°$ (*SI Appendix, Distribution Analysis of Solution Mass Measurement*). Broken lines represent the best-fitted model, assuming no cooperativity in binding. For omSpike (*F*) we assumed a maximum coverage of 2 ACE2 given no evidence for three bound ACE2 on a single spike trimer. Dashed lines in panels *B* and *C* (50 and 100 nM ACE2) show the expected shape of the mass distribution in the absence of cooperativity ($\delta\Delta G° = 0$), showing that a simple binding process cannot represent the data well.

sites (Fig. 3*D*, solid) does not lead to a significant improvement over a simple binding model, suggesting that the three RBD binding sites are independent for mACE2 binding. The affinity of spike is substantially weaker than that for RBD to mACE2, which is likely a result of additional steric constraints encountered in the full trimer, including the possibility of the RBD to be orientated in an "up" or "down" conformation (8).

Titrating ACE2 vs. spike results in improved peak separation due to the doubling in ligand mass (Fig. 3*B*). As previously, we observe an increase in ACE2 occupancy with increasing concentration. Contrary to our results with mACE2, however, we could not detect significant amounts of spike decorated with three ACE2 (*SI Appendix*, Fig. S8), indicating substantial steric inhibition of the final binding site in the presence of two bound ACE2. Comparison of the 50 nM ACE2 with 150 nM mACE2 traces shows similar relative amounts of free and single ACE2 bound spike, but much lower amounts of doubly bound ACE2 compared to mACE2, as was also reported previously (18). This binding behavior is indicative of negative cooperativity affecting binding of the second ACE2 to a singly occupied trimer.

To quantify these effects, we can turn to the same approach previously applied to mACE2, and fit the fractional occupancies as a function of ACE2 concentration to a simple model with the same interaction energy for all binding sites (Fig. 3*D*, dashed), as well as

Downloaded from https://www.pnas.org by 46.64.248.158 on October 11, 2024 from IP address 46.64.248.158.

a more complex one allowing for cooperativity (Fig. 3*D*, solid). The difference in the model's ability to reproduce the data (Fig. 3*D* solid vs dashed) demonstrates the statistical justification for including a cooperative component to the interaction. The global fit to the data yields K_D = 36 ± 6 nM (72 ± 12 nM in monomer concentration, SD represent the variation between biological replicates) for the first binding site which corresponds to a small increase in binding affinity compared with the affinity mACE2, and negative cooperativity of $\delta\Delta G^\circ$ = 0.6 ± 0.2 kcal mol^{-1} (the error is estimated from the difference between the fit shown in Fig. 3*E* and the maximum deviation of individual biological replicates). Given our results, we cannot exclude the possibility that ACE2 dimer can only weakly interact with a second RBD on the same wtSpike in a way that will partially prevent the binding of the next ACE2 dimer. However, given the small difference in the binding free energy between mACE2 binding and ACE2 (0.4 ± 0.1 kcal mol^{-1}) it is unlikely that intra-wtSpike avidity majorly contributes to ACE2-wtSpike affinity, as we would expect much larger differences in affinities owing to bivalent binding, as was suggested for the difference between IgG vs. Fab binding for the case of COVA1-18 (18). Repeating these experiments with omSpike exhibits similar behavior in terms of a maximum of two ACE2 bound, but binding of the second ACE2 now exhibits positive cooperativity, which can be seen in both the ability to reproduce the measured distributions and the titration data (Fig. 3 *E* and *F* and *SI Appendix*, Fig. S9). We obtain K_D = 88 ± 7 nM (176 ± 14 nM in monomer concentration) for the first binding site and positive cooperativity of $\delta\Delta G^\circ$ = −0.51 ± 0.07 kcal mol^{-1} (the SD represent the variations between two biological replicates)

These results quantify the interaction between ACE2 and spike trimers at a molecular level. We further validated that our stoichiometries and abundances represent the steady state distribution of the measured interactions (*SI Appendix*, Figs. S10 and S11). In addition, we did not detect any additional molecular species that may result from large-scale conformational changes, such as S1 shedding and transition to the postfusion conformation (40, 41) (*SI Appendix*, Figs. S7–S9). We attribute this observation to the stabilization of S1 and S2 interactions due to the mutation in the furin cleavage site and to the addition of two proline substitutions. We find that the 1:1 interaction is roughly two orders of magnitude weaker than previously reported using conventional surface-based assays. At the same time, ACE2 binds more strongly to spike than mACE2, suggesting additional stabilization for the full dimer. For both spike variants tested, we find significant cooperativity that switches from negative to positive from wtSpike to omSpike. Interestingly, the measured 1:1 molar affinity for omSpike is half as strong as for wtSpike, contrary to previous reports and the hypothesis that tighter interactions correlate with enhanced infectivity.

Induced Oligomerization Dominates the Interaction of Spike with Patient-Derived Antibodies. Given our observations of cooperativity and oligomerization for the ACE2–spike interactions, we wondered whether they play a role in antibody–spike interactions, given that antibodies provide dual binding potential, in principle similar to ACE2. In addition, we wondered whether these effects can help explain and understand differences in behaviors between patient-derived antibodies. We chose three previously studied antibodies (5) based on their representative behavior with respect to infectivity inhibition and receptor binding, differences between Fab fragments and full-length IgG, and the fact that they are reasonably representative of the types of behavior seen across a large range of antibodies: 1. Exhibiting only small differences between Fab and IgG for neutralization and binding (COVOX150). 2. Complete lack of neutralization for Fab (COVOX159). 3. Strongly enhanced neutralization and binding for the IgG over Fab (COVOX384). COVOX159 further differs from the other antibodies in that its epitope is in the NTD domain (Fig. 4 *A* and *B*, red), not in the RBD domain (Fig. 4 *A* and *B*, dark blue) and thus does not per se block binding to ACE2.

When adding 5 nM COVOX150 to wtSpike in a bilayer-based assay, almost all spike binds to a single antibody (Fig. 4*C* and *SI Appendix*, Fig. S11), indicative of a very strong 1:1 interaction. Nevertheless, the degree of induced oligomerization is comparatively weak, roughly matching that observed for ACE2 and omSpike, despite the latter exhibiting approximately two orders of magnitude weaker 1:1 affinity. Compared to COVOX150, COVOX159 induces oligomerization much more strongly, despite what appears to be a weaker 1:1 affinity, given that we can still observe free spike trimers at the same antibody concentration (Fig. 4*D*). The scatter plot of molecular mass and mobility now contains clear signatures of monomer, dimer, trimer, and tetramer of spike, with the dimer most abundant. For the first time, the distribution of mobilities is now dominated by oligomerized spike. Compared to COVOX150, there is a correlation between the abundance of multiple antibodies bound to a single spike trimer, and the degree of oligomerization. This behavior is similar for COVOX384 (Fig. 4*E*), which exhibits an almost identical distribution of species and mobilities to COVOX159. Oligomerization almost completely dominates the interaction when combining COVOX384 that binds the RBD in its closed conformation, with the HexaPro variant of spike (43), which shows lower binding affinity to soluble ACE2 receptor. These results may suggest that in solution the RBD of the HexaPro spike predominantly samples conformation that is more similar to its down position in terms of its binding propensity to ACE2 (Fig. 4*F* and Movies S4 and S5) (39).

From these data (*SI Appendix*, Figs. S12–S14), we can directly determine the cross-linked fraction of spike, which shows a clear trend from COVOX150 to COVOX159 and COVOX384 (Fig. 4*G*). We can also determine the amount of free and bound spike–antibody oligomers by fitting a set of Gaussian functions, constrained to the expected masses of the different oligomers (Fig. 4*H* and *SI Appendix*, Figs. S12–S14), from which we can extract the mole fraction of each species on the bilayer surface (Fig. 4*I*, gray). Based on these mole fractions and their variation with antibody concentration (*SI Appendix*, Fig. S15) we can use a comprehensive thermodynamic model that takes into consideration oligomerization on the membrane, its conformational degeneracy (44, 45) and the interactions between spike and soluble antibodies (*SI Appendix*, Eqs. **S1**–**S18**) to quantify the energetics, affinities, and degree of cooperativity for each antibody–spike system (Fig. 4*I*, red).

Fitting the detected mole fractions to the model allows us to determine both the three-dimentional (3D, soluble antibody to surface-bound spike) and the two-dimensional (2D, antibody-bound spike to free spike) standard free energies of interaction (*SI Appendix*, Table S2). While all antibodies exhibit primary 3D affinities in the 1 to 5 nM regime (*SI Appendix*, Table S2), both COVOX159 and COVOX384 oligomerize spike much more strongly than COVOX150, as seen by the ratio between their 3D and 2D K_Ds (Fig. 4*J*). The observed behavior is directly linked to the inhibition efficacy of the antibodies. COVOX150, which oligomerizes weakly but binds to the RBD, exhibits the overall weakest IC50 of the three antibodies tested, with small differences between binding, inhibition, Fab, and IgG (discussed further below). COVOX384 binds to the RBD and oligomerizes strongly, making it one of the most potent antibodies (5). Remarkably,

Downloaded from https://www.pnas.org by 46.64.248.158 on October 11, 2024 from IP address 46.64.248.158.

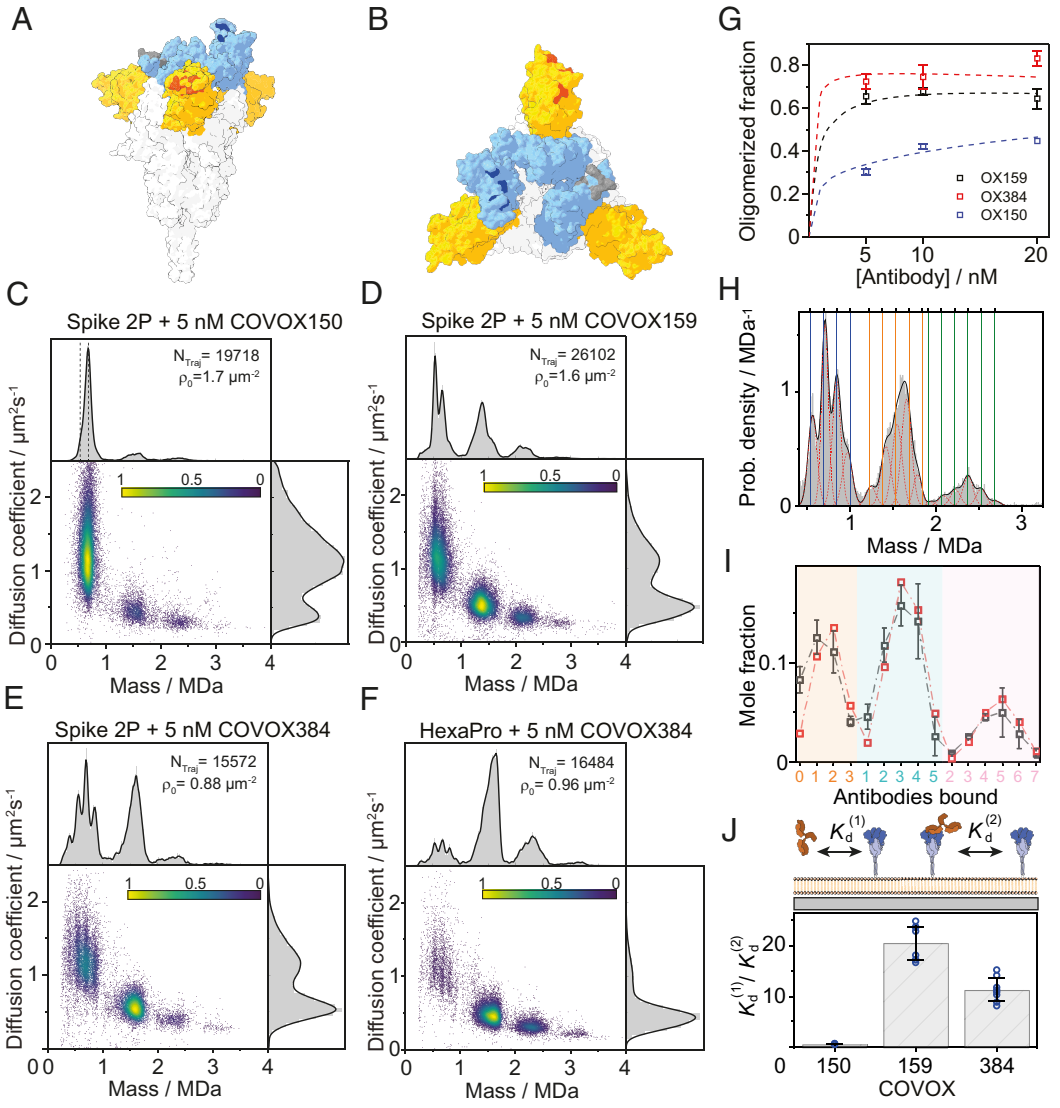

Fig. 4. Induced oligomerization by patient-derived antibodies correlates with enhanced inhibition of infection by full IgGs. (*A* and *B*) Side and *Top* view of the spike trimer based on PDB entry 6vsb (8, 42) with the NTD (yellow) and RBD (light blue) domains highlighted. The binding locations of the different antibodies are highlighted based on their identified interactions (5). Gray, dark blue, and red correspond to COVOX384 (down state of the RBD), COVOX150 (up state of the RBD), and COVOX159, respectively. (*C*–*E*) Two-dimensional plots of diffusion coefficient *vs.* mass for equilibrated tethered wtSpike (stabilized by two proline substitutions, 2P) with added 5 nM of (*C*) COVOX150, (*D*) COVOX159, and (*E*) COVOX384. The number of trajectories sampled for each solution condition and the measured initial surface density of spike on the supported lipid bilayer are indicated for each plot. Dashed lines in (*C*) correspond to the expected masses of spike and spike bound to one antibody. (*F*) COVOX384 interacting with tethered wtSpike, stabilized by six proline substitutions (HexaPro). (*G*) Mole fraction of spike trimers in higher oligomeric states as a function of the concentration of added antibody to the solution. Values were extracted by counting the number of trajectories for each oligomeric state relative to the total number of detected trajectories while considering the stoichiometry of each state. Symbols and error bars indicate the average values and SD of two independent measurements (except for the case of COVOX150 at 20 nM that includes one repetition). Colored dashed lines correspond to our fitted two-dimensional thermodynamic model (*SI Appendix*, Eqs. **S1**–**S18**). (*H*) Representative normalized mass distribution of equilibrated, tethered wtSpike, with 10 nM COVOX159, fitted to a sum of individual Gaussian functions constrained around the expected mass of the different spike:antibody stoichiometries. The black line corresponds to the sum of the Gaussian functions and red dotted lines to the individual Gaussian fits. Dashed vertical lines indicate the masses of the expected wtSpike:antibody complexes, where blue, orange, and green correspond to complexes containing one, two, or three spike trimers, respectively. (*I*) Mole fractions of individual complexes (gray symbols), calculated from the fitted relative areas of the individual Gaussian functions from *H*. The *x*-axis corresponds to the number of bound COVOX159 antibodies to an individual spike trimer (orange), to two trimers (cyan), or to three trimers (pink). Error bars indicate the variation between two independent experiments. Red symbols correspond to the predicted mole fractions based on our globally fitted two-dimensional thermodynamic model. (*J*) Ratio of binding affinity from solution, $K_D^{(1)}$, to its two-dimensional affinity for cross-linking, $K_D^{(2)}$. Both values were calculated from the fitted interaction free energies ($\epsilon^{\circ}_{1,2}$ in *SI Appendix*, Eqs. **S15** and **S17**). Average values for the different antibodies are indicated by the height of each column, where the statistical variation of the fitted ratio values (blue symbols) was calculated by repeating the fitting procedure (global fitting for 5,10, and 20 nM of antibody simultaneously) for different sets of concentrations and repetitions (three different concentrations of antibody per set and two independent repetitions for each concentration, except for 20 nM COVOX150). SD are indicated by black error bars.

COVOX159 does not bind to the RBD region, and thus does not inhibit ACE2 binding by occupying the RBD, yet exhibits strong inhibition, which is likely entirely attributable to its ability to oligomerize spike on the surface of the virus. In fact, our results show that ACE2 still binds successfully to a COVOX159-prebound spike in solution (*SI Appendix*, Fig. S16), which suggest that 1:1 binding affinity does not play a role in its neutralization.

Consequences of Induced Oligomerization at Viral Receptor Densities. Our approach is limited to spike densities on the membrane up to 2 μm^{-2} due to the need to separately visualize and quantify individual spike complexes in a diffraction-limited imaging system. The density on the surface of the virus, however, is about three orders of magnitude higher than the experimental limit in this study, with structural flexibility that may further

Downloaded from https://www.pnas.org by 46.64.248.158 on October 11, 2024 from IP address 46.64.248.158.

facilitate multivalent interactions (37, 46). Having quantified the relevant energetics at the molecular level, we can now use the thermodynamic parameters, in this case taken from the spike–COVOX159 or wtSpike–ACE2 systems, to deduce macroscopic observables such as the fraction of bound RBD and the fraction of bound spike as a function of ligand concentration, multivalency, and different spike surface densities.

The thermodynamic model, predicts a >2 orders of magnitude improvement in RBD occupancy (*SI Appendix*, Fig. S17) or bound spike fraction (Fig. 5 *A* and *B*) for an oligomerization-prone binder compared to the monomer (black curves) when surface densities approach the density of spike proteins on the virus surface for both ACE2 and COVOX159 (Fig. 5 *A* and *B*). This effect is strongest at low ligand concentrations ($<K_{D1:1}$), where oligomerization dominates and improves spike occupancy even at extremely low ligand concentrations (Fig. 5*C*). At higher ligand concentrations the oligomerization capacity is already saturated and limited by free spike surface density, therefore the binding becomes dominated by the 3D affinity, which leads to the observed convergence of binding curves (*SI Appendix*, Fig. S17).

Finally, we show that cooperative oligomerization enhances spike binding to a membrane surface containing different densities of ACE2 (Fig. 5*D*). Here, we assumed the interaction parameters of omSpike, where each spike trimer can bind up to two ACE2, and the second binding event includes positive cooperativity. In this case spike and ACE2 can form linear oligomers on the membrane surface. Similar to previous results and depending on ACE2 surface density, oligomerization results in more than one order of magnitude enhancement of spike affinity. The enhancement is maximal at a concentration much lower than the modeled fundamental K_D (82 nM), while at higher concentrations than the fundamental K_D, the trend is inverted owing to the larger number of binding sites for un-oligomerized ACE2. In all cases, our calculations reveal the role of cooperativity and multivalency in strengthening the apparent affinity up to several orders of magnitude compared to the fundamental K_D of the monomeric subunits. The increase in the binding free energy gain resulting from induced oligomerization is a function of the 2D affinity (oligomerization propensity) and the chemical potential of the free tethered component and therefore its surface density. Thus, we expect the binding enhancement to be most prominent at high surface densities and solutions concentrations lower than the solution K_D, while at high concentration this enhancement factor is lower since the ligand is already saturating the tethered receptor owing to its 3D affinity.

Discussion

Our results have significant implications for our quantitative molecular understanding of spike–ACE2 and spike–antibody interactions specifically, but also for oligomeric protein–protein interactions more broadly. The ability of MP to disentangle protein–protein interactions and avidity on a subunit-by-subunit level reveals a much more nuanced picture compared to that emerging from bulk biophysical and structural methods. Our observed ACE2-RBD affinity of 28 ± 9 nM fits well into the range of reported values (17 to 75 nM) (8, 12, 21, 24, 32–34). However, we find 3- and 6-times weaker binding to spike for both variants tested contrary to previous reports, which reported up to 100-fold enhancement of the interaction strength (12), down to apparent K_Ds of 0.015 to 3 nM (12, 25, 35, 36) when both ACE2 and spike are multivalent. A weaker interaction strength, however, is expected for spike in the absence of intramolecular avidity, given that the RBD can occupy an up or down position, only the latter of which is capable of binding ACE2. A likely explanation for this difference, and for many of the discrepancies between our observed affinities and those reported with bulk methods, can be attributed to the fact that bulk characterization can inadvertently allow for intermolecular interactions that have not been taken into account. Thus, our results agree well with assays using monomeric

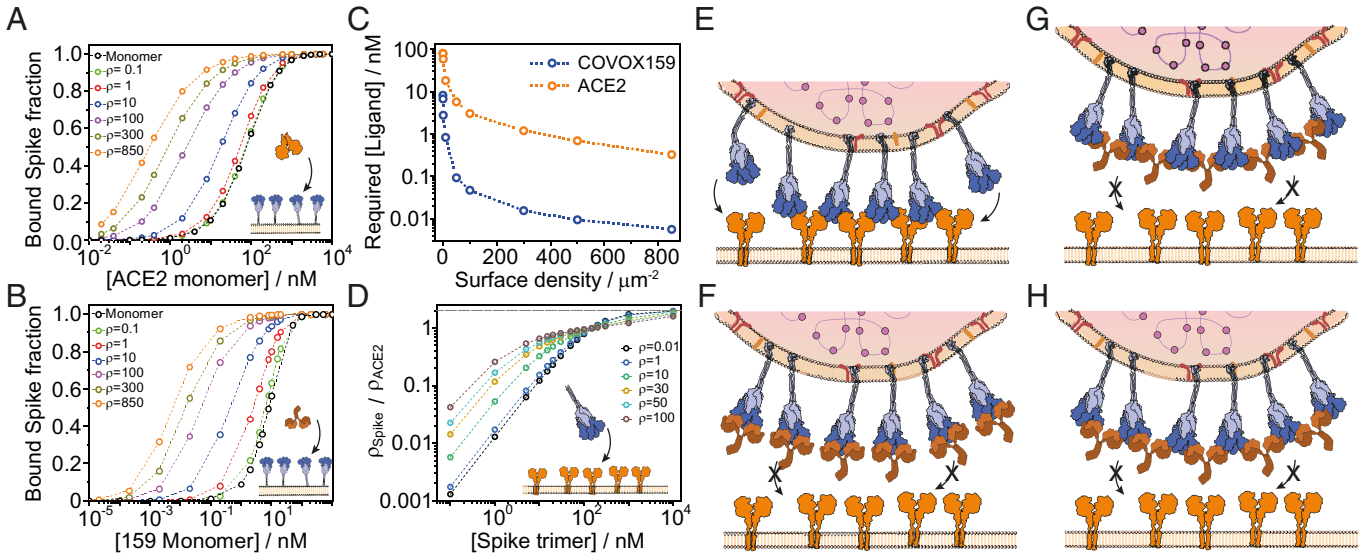

Fig. 5. Induced oligomerization enhances binding of multivalent ligands to their surface multivalent receptors. (*A* and *B*) Molar fraction of spike trimers bound to at least one ACE2 (*A*) or COVOX159 antibody (*B*) for different spike surface densities calculated from experimentally determined affinities. The monomer binding curve (black) corresponds to no induced oligomerization. (*C*) Required ligand solution concentration resulting in half of spike bound to at least one ligand as a function of spike surface density. (*D*) Normalized surface density of spike bound to a surface containing different densities of diffusive ACE2 dimers as a function of spike solution concentration. (*E–H*) Mechanisms of binding and inhibition of SARS-CoV-2 to its host cell-surface. (*E*) Induced oligomerization of spike and ACE2 during cell-surface binding. (*F*) Inhibition of SARS-CoV-2 binding by blocking the ACE2 binding site by competitive antibodies. (*G*) Blocking cell-surface attachment without affecting the ACE2 binding site by spike oligomerization alone. (*H*) The most potent antibodies combine ACE2 binding site blocking with spike cross-linking in their mechanism of action.

Downloaded from https://www.pnas.org by 46.64.248.158 on October 11, 2024 from IP address 46.64.248.158.

constructs, but deviate substantially with those where oligomeric ligands are added to a surface covered with receptors.

We show that the multivalency of both spike and ACE2 plays an important role in their interaction. Our observations of ACE2-induced oligomerization of spike both in solution and on lipid bilayers (as a function of solution concentrations or surface densities, *SI Appendix*, Figs. S21–S23) provide insight into its importance for both cellular binding and internalization, as well as inhibition. Previous reports have demonstrated two orders of magnitude improvement in efficacy of dimeric over monomeric ACE2 in the context of viral inhibition (10–12). This, could a priori be explained by intraspike avidity where a dimeric ACE2 can bind to two RBD on the same spike, resulting in enhanced affinity. Yet, despite the anticipated high stability of such a complex, the associated structure has never been reported. Additionally, intraspike avidity would block extended spike oligomerization, because it requires at least two interspike interactions per trimer. Our results allow us to rationalize the molecular mechanism underlying the inhibitory efficacy of multivalent ligands, while being in quantitative agreement with previously reported enhancement in inhibition. Furthermore, the ability of ACE2 to oligomerize spike makes it essentially impossible for the virus to detach from the cellular surface due to the associated avidity effects and drives receptor clustering, which is associated with signaling for internalization, inducing membrane curvature and ultimately fusion (47, 48).

In contrast to standard 1:1 affinities, we resolve the stoichiometries of the interaction and their relative abundances, which provide insight into cooperative effects. We find binding to be independent for mACE2 and wtSpike, but substantial effects for ACE2 that changes with the spike variant. Contrary to previous reports (12, 25), we find that the 1:1 affinity of the Omicron variant is weaker than that of the original Wuhan-Hu-1 strain, but exhibits a switch from negative (Wuhan) to positive (Omicron) cooperativity for higher binding stoichiometries. Combining these results with measurements on a lipid bilayer, we could connect the observed positive cooperativity to an increased oligomerization propensity. This combination will lead to preferential binding to tissues and cells with higher ACE2 density, where multiple interactions with ACE2 are favored both for surface attachment (Fig. 5 *D* and *E*) and possibly for the priming of the postfusion configuration as suggested by simulations (49).

Our results with patient-derived antibodies reveal a hierarchy of interactions and help explain mechanisms of virus neutralization. COVOX150 exhibits strong binding to the RBD but weak oligomerization (Fig. 5*F*), leading to relatively weak inhibition (IC50 = 0.15 nM) (5). COVOX159 exhibits slightly better inhibition (IC50 = 0.033 nM) (5) despite its slightly weaker affinity and leaving the RBD untouched, which likely arises from its ability to efficiently induce the oligomerization of spike trimers on the viral surface. The binding mechanism of COVOX159 emphasizes the potential of induced oligomerization in virus neutralization, as binding alone, even at a 3:1 stoichiometry, did not prevent cobinding of ACE2. The best-performing antibody (COVOX384) combines RBD binding and oligomerization for overall maximal inhibition (IC50 = 0.013 nM) (5), despite similar 1:1 binding affinity to the other antibodies. The dramatic improvements in target occupancy achievable at low ligand concentrations (Fig. 5 *A* and *B*), the ability to achieve an inhibitory effect without targeting the RBD, and the ability to enhance the effect of binding to the RBD (coupled with the intrinsically dimeric structure of antibodies) raises the possibility that induced oligomerization is a more general inhibitory mechanism used by the immune system. However, our data are not able to identify the mechanism by which infection is inhibited, which could be caused by clustering of spike on the viral membrane in orientations that does not suitable for ACE2 binding, cross-linking spike on different virions as observed previously for HIV using dimeric IgA (50), changes to the RBD dynamics, or aggregation coupled with partial occupancy of the RBDs.

Taken together, our results reveal the nature and importance of induced oligomerization for both virus-cell binding and inhibition by antibodies. They demonstrate that models solely based on 1:1 interactions fail to identify the molecular details that are responsible for fundamental differences in infectivity and inhibition. Instead, propensity to induce oligomerization is as important if not more important than the strength of the molecular interfaces defining the fundamental interaction. Our results also raise the question to which degree oligomerization represents a more fundamental mechanism driving interactions and effects such as tropism. In addition, our results raise the possibility that these interactions are in fact fundamental to the way antibodies function in the context of their unique, effectively dimeric structure. Importantly, these effects do not rely on multivalency alone, they require geometric restrictions, which in this case prevent both ACE2 and antibodies to bind two sites within the oligomeric target (intramolecular avidity) and instead drive oligomerization (intermolecular avidity), an effect that could be leveraged in the rational design of future therapeutics.

Material and Methods

An extended *SI Appendix, Material and Methods* section is provided, and includes the following: The expression and purification procedure for wtSpike 2P, omSpike 2P as well as monomeric and dimeric ACE2; The measurement procedure and data analysis used to perform the solution-based MP experiments for the characterization of the interactions between ACE2 and spike–RBD, wtSpike and omSpike with monomeric and dimeric ACE2 and the simultaneous interaction of wtSpike with dimeric ACE2 and antibody COVOX159; A complete description of the globally fitted thermodynamic models for each case is further provided; Experimental procedures for supported lipid bilayer preparation and dynamic-MP measurements; Dynamic MP image analysis and single-particle trajectory analysis for extracting the particle mass and diffusion coefficient; Extracting the relative abundances of molecular species on the supported lipid bilayers and fitting the two-dimensional thermodynamic distributions. A specific section addresses the observed contrast changes owing to optical path differences between the glass surface and spike on a supported lipid bilayer. Last, we include a complete thermodynamic model for 2D antibody-induced spike oligomerization on supported lipid bilayers that includes: the interaction model for the spike–antibody system, parameters for the interactions of antibodies 159, 384, and 150 with spike, and comparison between monovalent and divalent binding curves.

Data, Materials, and Software Availability. The raw data and analyzed data required to reproduce the figures in the paper have been deposited in University of Oxford Research Archive (ora.ox.ac.uk), including:-.mp and .tdms files for MP movies, -analysed results as .csv and .h5 files and text files in the form of .out and .txt files, -python code (.py and .ipynb) for data analysis and figures generation. The title of the dataset is: "Oligomerisation-driven avidity correlates with SARS-CoV-2 cellular binding and inhibition" (DOI: 10.5287/ora-1zppvdavr) (51).

ACKNOWLEDGMENTS. The pCAGGS expression plasmid encoding the Wuhan-hu-1 2P spike trimer and the vector encoding the Wuhan-hu-1 spike RBD were kindly provided by the Krammer Laboratory, Department of Microbiology, Icahn School of Medicine at Mount Sinai, New York. The pHL-sec vector encoding Omicron 2P spike was a kind gift from the Townsend Laboratory, Weatherall Institute of Molecular Medicine, University of Oxford. pcDNA3-sACE2-WT(732)-IgG1 was a gift from Erik Procko (Addgene plasmid #154104; http://n2t.net/addgene:154104; RRID:Addgene_154104). European Research Council PHOTOMASS 819593 (P.K.) Engineering and Physical Sciences Research Council EP/T03419X/1 (P.K.) UKRI Future Leaders Fellowship MR/V02213X/1 (W.B.S.) University of Oxford's COVID-19

Downloaded from https://www.pnas.org by 46.64.248.158 on October 11, 2024 from IP address 46.64.248.158.

Research Response Fund (W.B.S. and P.K.) European Molecular Biology Organization (EMBO) Postdoctoral Fellowship ALTF 198-2020 (R.A.) Oak Foundation (J.M. and G.R.S.) Wellcome trust SEACOVARIANTS consortium 226120/Z/22/Z (J.M., D.I.S., and G.R.S.) Wellcome Trust Centre for Human Genetics 090532/Z/09/Z (J.M. and G.R.S.) The Chinese Academy of Medical Sciences Innovation Fund for Medical Science, China 2018- I2M-2-002 (L.C., J.M., and G.R.S.) Fast Grants, Mercatus Center, NIH Research Biomedical Research Centre Funding Scheme (G.R.S.) Medical Research Council (MR/N00065X/1) (D.I.S.) Schmidt Futures, and Red Avenue Foundation (G.R.S.) Wellcome Trust PhD Programme 203853/Z/16/Z (J.L.P.B.) Oxford Glycobiology Endowment (N.Z.) Biotechnology and Biological Sciences Research Council BB/V011456/1 (J.L.P.B. and W.B.S.)

Author affiliations: [a]Physical and Theoretical Chemistry, Department of Chemistry, University of Oxford, Oxford OX1 3QZ, United Kingdom; [b]The Kavli Institute for Nanoscience Discovery, Dorothy Crowfoot Hodgkin Building, University of Oxford, Oxford OX1 3QU, United Kingdom; [c]Department of Biochemistry, University of Oxford, Oxford OX1 3QU, United Kingdom; [d]Department of Physics, Durham University, Durham DH1 3LE, United Kingdom; [e]Wellcome Centre for Human Genetics, Nuffield Department of Medicine, University of Oxford, Oxford OX3 7BN, United Kingdom; [f]Chinese Academy of Medical Science Oxford Institute, University of Oxford, Oxford OX3 7FZ, United Kingdom; [g]Division of Emerging Infectious Disease, Research Department, Faculty of Medicine Siriraj Hospital, Mahidol University, Bangkoknoi, Bangkok 10700, Thailand; [h]Division of Structural Biology, Wellcome Centre for Human Genetics, University of Oxford, Oxford OX3 7BN, United Kingdom; [i]Diamond Light Source (United Kingdom), Harwell Science and Innovation Campus, Didcot OX110DE, United Kingdom; and [j]Oxford University Hospitals National Health Service Foundation Trust, Oxford OX3 7JH, United Kingdom

Author contributions: R.A., A.O., J.L.P.B., W.B.S., and P.K. designed research; R.A., A.O., S.A.B., M.S.K., F.S., L.S.P.R., and M.T.D. performed research; M.H., S.V., J.B., M. Hill, L.C., W.D., P.S., J.M., D.Z., D.I.S., G.R.S., and N.Z. contributed new reagents; R.A., A.O., W.B.S., and P.K. analyzed data; R.A. and P.K. wrote the original draft; L.S.P.R. and M.D. computational support; M. Hensen, S.V., J.B., M. Hill, and N.Z. supply ACE2 and spike constructs; L.C., W.D., P.S., J.M., D.Z., D.I.S., and G.R.S. supply of antibodies; and R.A., J.L.P.B., W.B.S., and P.K. wrote the paper.

Competing interest statement: P.K. is a nonexecutive director, shareholder of and consultant to Refeyn Ltd., J.L.P.B. and W.B.S. are shareholders of and consultants to Refeyn Ltd. W.B.S. and P.K. received the University of Oxford's COVID-19 Research Response Fund. P.K. has filed a patent for the contrast enhancement methodology and its application to mass measurement of single biomolecules. G.R.S. is on the GSK Vaccines Scientific Advisory Board, a founder shareholder of RQ biotechnology and Jenner investigator. Oxford University holds intellectual property related to the Oxford-AstraZeneca vaccine.

1. J. Mercer, M. Schelhaas, A. Helenius, Virus entry by endocytosis. *Annu. Rev. Biochem.* **79**, 803–833 (2010), 10.1146/annurev-biochem-060208-104626.
2. D. J. Schofield, N. J. Dimmock, J. R. Stephenson, Variations in the neutralizing and haemagglutination-inhibiting activities of five influenza A virus-specific IgGs and their antibody fragments. *J. Gen. Virol.* **78**, 2431–2439 (1997), 10.1099/0022-1317-78-10-2431.
3. J. S. Klein, P. J. Bjorkman, Few and far between: How HIV may be evading antibody avidity. *PLoS Pathog.* **6**, e1000908 (2010), 10.1371/journal.ppat.1000908.
4. C. O. Barnes *et al.*, Structures of human antibodies bound to SARS-CoV-2 Spike reveal common epitopes and recurrent features of antibodies. *Cell* **182**, 828–842.e16 (2020), 10.1016/j.cell.2020.06.025.
5. W. Dejnirattisai *et al.*, The antigenic anatomy of SARS-CoV-2 receptor binding domain. *Cell* **184**, 2183–2200.e22 (2021), 10.1016/J.CELL.2021.02.032.
6. R. Yan *et al.*, Structural basis for the recognition of SARS-CoV-2 by full-length human ACE2. *Science* **367**, 1444–1448 (2020), 10.1126/science.abb2762.
7. H. Wu *et al.*, Ultra-potent antibodies against respiratory syncytial virus: Effects of binding kinetics and binding valence on viral neutralization. *J. Mol. Biol.* **350**, 126–144 (2005), 10.1016/j.jmb.2005.04.049.
8. D. Wrapp *et al.*, Cryo-EM structure of the 2019-nCoV spike in the prefusion conformation. *Science* **367**, 1260–1263 (2020), 10.1126/science.abb2507.
9. V. Monteil *et al.*, Inhibition of SARS-CoV-2 infections in engineered human tissues using clinical-grade soluble human ACE2. *Cell* **181**, 905–913.e7 (2020), 10.1016/j.cell.2020.04.004.
10. K. K. Chan *et al.*, Engineering human ACE2 to optimize binding to the spike protein of SARS coronavirus 2. *Science* **369**, 1261–1265 (2020), 10.1126/science.abc0870.
11. T. Xiao *et al.*, A trimeric human angiotensin-converting enzyme 2 as an anti-SARS-CoV-2 agent. *Nat. Struct. Mol. Biol.* **28**, 202–209 (2021), 10.1038/s41594-020-00549-3.
12. W. Yin *et al.*, Structures of the Omicron spike trimer with ACE2 and an anti-Omicron antibody. *Science* **375**, 1048–1053 (2022), 10.1126/science.abn8863.
13. R. Yan *et al.*, Structural basis for bivalent binding and inhibition of SARS-CoV-2 infection by human potent neutralizing antibodies. *Cell Res.* **31**, 517–525 (2021), 10.1038/s41422-021-00487-9.
14. H. M. Callaway *et al.*, Bivalent intra-spike binding provides durability against emergent Omicron lineages: Results from a global consortium. *Cell Rep.* **42**, 112014 (2023), 10.1016/j.celrep.2023.112014.
15. C. A. Jette *et al.*, Broad cross-reactivity across sarbecoviruses exhibited by a subset of COVID-19 donor-derived neutralizing antibodies. *Cell Rep.* **36**, 109760 (2021), 10.1016/j.celrep.2021.109760.
16. C. O. Barnes *et al.*, SARS-CoV-2 neutralizing antibody structures inform therapeutic strategies. *Nature* **588**, 682–687 (2020), 10.1038/s41586-020-2852-1.
17. T. J. El-Baba *et al.*, Uncovering the role of N-Glycan occupancy on the cooperative assembly of spike and angiotensin converting enzyme 2 complexes: Insights from glycoengineering and native mass spectrometry. *J. Am. Chem. Soc.* **145**, 8021–8032 (2023), 10.1021/jacs.3c00291.
18. V. Yin *et al.*, Probing affinity, avidity, anticooperativity, and competition in antibody and receptor binding to the SARS-CoV-2 spike by single particle mass analyses. *ACS Cent. Sci.* **7**, 1863–1873 (2021), 10.1021/acscentsci.1c00804.
19. L. Radić *et al.*, Bispecific antibodies combine breadth, potency, and avidity of parental antibodies to neutralize sarbecoviruses. *iScience* **26**, 106540 (2023), 10.1016/j.isci.2023.106540.
20. S. H. Kim *et al.*, SARS-CoV-2 evolved variants optimize binding to cellular glycocalyx. *Cell Rep. Phys. Sci.* **4**, 101346 (2023), 10.1016/j.xcrp.2023.101346.
21. E. Cameroni *et al.*, Broadly neutralizing antibodies overcome SARS-CoV-2 Omicron antigenic shift. *Nature* **602**, 664–670 (2022), 10.1038/s41586-021-04386-2.
22. J. Huo *et al.*, A delicate balance between antibody evasion and ACE2 affinity for Omicron BA.2.75. *Cell Rep.* **42**, 111903 (2023), 10.1016/j.celrep.2022.111903.
23. L. Li *et al.*, Structural basis of human ACE2 higher binding affinity to currently circulating Omicron SARS-CoV-2 sub-variants BA.2 and BA.1.1. *Cell* **185**, 2952–2960.e10 (2022), 10.1016/j.cell.2022.06.023.
24. P. Han *et al.*, Receptor binding and complex structures of human ACE2 to spike RBD from omicron and delta SARS-CoV-2. *Cell* **185**, 630–640.e10 (2022), 10.1016/j.cell.2022.01.001.
25. D. Mannar *et al.*, SARS-CoV-2 Omicron variant: Antibody evasion and cryo-EM structure of spike protein–ACE2 complex. *Science* **375**, 760–764 (2022), 10.1126/science.abn7760.
26. L. Wu *et al.*, SARS-CoV-2 Omicron RBD shows weaker binding affinity than the currently dominant Delta variant to human ACE2. *Signal Transduct. Target. Ther.* **7**, 8 (2022), 10.1038/s41392-021-00863-2.
27. M. I. Barton *et al.*, Effects of common mutations in the sars-cov-2 spike rbd and its ligand the human ace2 receptor on binding affinity and kinetics. *Elife* **10**, e70658 (2021), 10.7554/ELIFE.70658.
28. G. Young *et al.*, Quantitative mass imaging of single biological macromolecules. *Science* **360**, 423–427 (2018), 10.1126/science.aar5839.
29. E. D. B. Foley, M. S. Kushwah, G. Young, P. Kukura, Mass photometry enables label-free tracking and mass measurement of single proteins on lipid bilayers. *Nat. Methods* **18**, 1247–1252 (2021), 10.1038/s41592-021-01261-w.
30. T. Heermann, F. Steiert, B. Ramm, N. Hundt, P. Schwille, Mass-sensitive particle tracking to elucidate the membrane-associated MinDE reaction cycle. *Nat. Methods* **18**, 1239–1246 (2021), 10.1038/s41592-021-01260-x.
31. F. Soltermann *et al.*, Quantifying protein-protein interactions by molecular counting with mass photometry. *Angew. Chem. Int. Ed. Engl.* **132**, 10866–10871 (2020), 10.1002/ange.202001578.
32. J. Shang *et al.*, Structural basis of receptor recognition by SARS-CoV-2. *Nature* **581**, 221–224 (2020), 10.1038/s41586-020-2179-y.
33. C. Laffeber, K. de Koning, R. Kanaar, J. H. G. Lebbink, Experimental evidence for enhanced receptor binding by rapidly spreading SARS-CoV-2 variants. *J. Mol. Biol.* **433**, 167058–167058 (2021), 10.1016/J.JMB.2021.167058.
34. P. Supasa *et al.*, Reduced neutralization of SARS-CoV-2 B.1.1.7 variant by convalescent and vaccine sera. *Cell* **184**, 2201–2211.e7 (2021), 10.1016/J.CELL.2021.02.033.
35. S. Ozono *et al.*, SARS-CoV-2 D614G spike mutation increases entry efficiency with enhanced ACE2-binding affinity. *Nat. Commun.* **12**, 848 (2021), 10.1038/s41467-021-21118-2.
36. A. C. Walls *et al.*, Structure, function, and antigenicity of the SARS-CoV-2 spike glycoprotein. *Cell* **181**, 281–292.e6 (2020), 10.1016/j.cell.2020.02.058.
37. Z. Ke *et al.*, Structures and distributions of SARS-CoV-2 spike proteins on intact virions. *Nature* **588**, 498–502 (2020), 10.1038/s41586-020-2665-2.
38. Y. Wu, J. Vendome, L. Shapiro, A. Ben-Shaul, B. Honig, Transforming binding affinities from three dimensions to two with application to cadherin clustering. *Nature* **475**, 510–513 (2011), 10.1038/nature10183.
39. S. A. Burnap, W. B. Struwe, Mass photometry reveals SARS-CoV-2 spike stabilisation to impede ACE2 binding through altered conformational dynamics. *Chem. Commun.* **58**, 12939–12942 (2022), 10.1039/D2CC04711J.
40. A. C. Walls *et al.*, Unexpected receptor functional mimicry elucidates activation of coronavirus fusion. *Cell* **176**, 1026–1039.e15 (2019), 10.1016/j.cell.2018.12.028.
41. D. J. Benton *et al.*, Receptor binding and priming of the spike protein of SARS-CoV-2 for membrane fusion. *Nature* **588**, 327–330 (2020), 10.1038/s41586-020-2772-0.
42. H. Woo *et al.*, Developing a fully glycosylated full-length SARS-COV-2 spike protein model in a viral membrane. *J. Phys. Chem. B* **124**, 7128–7137 (2020), 10.1021/acs.jpcb.0c04553.
43. C.-L. Hsieh *et al.*, Structure-based design of prefusion-stabilized SARS-CoV-2 spikes. *Science* **369**, 1501–1505 (2020), 10.1126/science.abd0826.
44. R. J. Goldberg, A theory of antibody-antigen reactions. I. Theory for reactions of multivalent antigen with bivalent and univalent antibody. *J. Am. Chem. Soc.* **74**, 5715–5725 (1952), 10.1021/ja01142a045.
45. B. Goldstein, A. S. Perelson, Equilibrium theory for the clustering of bivalent cell surface receptors by trivalent ligands. Application to histamine release from basophils. *Biophys. J.* **45**, 1109–1123 (1984), 10.1016/S0006-3495(84)84259-9.
46. B. Turoňová *et al.*, In situ structural analysis of SARS-CoV-2 spike reveals flexibility mediated by three hinges. *Science* **370**, 203–208 (2020), 10.1126/science.abd5223.
47. N. C. Hartman, J. T. Groves, Signaling clusters in the cell membrane. *Curr. Opin. Cell Biol.* **23**, 370–376 (2011), 10.1016/j.ceb.2011.05.003.
48. Y. Yuan *et al.*, Single-molecule super-resolution imaging of T-cell plasma membrane CD4 redistribution upon HIV-1 binding. *Viruses* **13**, 142 (2021), 10.3390/v13010142.
49. A. J. Pak, A. Yu, Z. Ke, J. A. G. Briggs, G. A. Voth, Cooperative multivalent receptor binding promotes exposure of the SARS-CoV-2 fusion machinery core. *Nat. Commun.* **13**, 1002 (2022), 10.1038/s41467-022-28654-5.
50. D. J. Stieh *et al.*, Aggregate complexes of HIV-1 induced by multimeric antibodies. *Retrovirology* **11**, 78 (2014), 10.1186/s12977-014-0078-8.
51. R. Asor, Data and Code for "Oligomerization-driven avidity correlates with SARS-CoV-2 cellular binding and inhibition". Oxford Research Archive. https://doi.org/10.5287/ora-1zppvdavr. Deposited 30 August 2024.

Downloaded from https://www.pnas.org by 46.64.248.158 on October 11, 2024 from IP address 46.64.248.158.